Multi-scale simulation of droplet-droplet interaction and coalescence

Ndivhuwo M. Musehane[a,b], Oliver F. Oxtoby[a,*], B. Daya Reddy[b]

[a]*Aeronautic Systems, Council for Scientific and Industrial Research,*
P.O. Box 395, Pretoria, 0001, South Africa
[b]*Department of Mathematics and Applied Mathematics and Centre for Research in*
Computational and Applied Mechanics, University of Cape Town, Rondebosch, 7701, South
Africa

Abstract

In this work, droplet-droplet interaction is modelled using a multi-scale approach which couples multiphase flow simulation using a volume of fluid method to a surface thin film model operating on the sub-grid scale. The volume of fluid model is based on a multiple marker method with a smoothed surface tension calculation, and a thin film model is derived to simulate film drainage using a Reynolds equation approach. A novel method of coupling the two allows for the prediction of coalescence or rebound of colliding droplets essentially from first principles, relying only on a critical film thickness parameter. The model is implemented using the open source tool set OpenFOAM and tested against experimental results of colliding hydrocarbon droplets from the literature. It is found to produce accurate interface deformation results for the duration of the collision, and to consistently predict the outcome of the collision process.

Keywords: Coalescence, Thin film, Droplets, VOF, Reynolds equation, Multiphase

1. Introduction

This work consists of the development and validation of a reduced-order surface thin film model coupled to a multiple-marker volume of fluid (VOF) method [1, 2], to model droplet-droplet interactions and their resultant coalescence or rebound. Droplet-droplet interaction is found in various industrial applications involving sprays, such as turbojet and rocket engines [3], internal combustion engines [4], and spray drying [5]. The resulting coalescence events influence the hydrodynamic and fluid transport phenomena that govern the overall flow behaviour, affecting the droplet size distribution and shape which in turn influ-

---

[*]Corresponding author
Email address: `ooxtoby@csir.co.za` (Oliver F. Oxtoby)

ence the overall optimal operating conditions. However, there are difficulties in modelling the collision process computationally.

Several multiphase flow modelling techniques are available to deal with droplets entrained in a fluid. These methods differ in their description and treatment of the droplet-fluid interface. Euler-Euler and Euler-Lagrange type methods model the distributed droplets as a continuous field, or as idealised point particles, respectively, and therefore need to employ empirical correlations when modelling coalescence [6]. They are therefore heavily reliant on prior knowledge and assumptions about the flow structure. On the other hand, interface tracking methods [7] can be computationally intensive due to the mesh deformations required and, due to mesh entanglement, demand great algorithmic complexity to capture large topology changes that result when droplets interact. The interface capturing VOF method provides a direct numerical simulation (DNS) approach to modelling droplet-droplet interactions. Although it is straightforward to implement computationally it has two major drawbacks: Firstly, inaccuracies in modelling the surface tension force [8, 9, 10, 11], and secondly the inherent nonphysical coalescence that results when two particles are very close to each other [12, 2]. It is necessary to prevent the nonphysical merging of interfaces so that particle rebound can be modelled correctly. Nobari *et al.* [7] introduced a 'ghost cell' method to achieve this, imposing a Dirichlet boundary condition on the volume fraction field along the collision plane which is changed to a symmetry condition in order to merge the droplets. This method is, however, restricted to head-on collisions. To handle the general case, Coyajee and Boersma [2] developed the multiple marker method, where separate droplets are treated as if they are different, immiscible materials. Various studies have demonstrated excellent agreement between numerical computation and experimental snapshots of colliding bubbles, provided the moment of coalescence is correctly imposed [13, 14, 15, 16].

The occurrence of coalescence and hence the outcome of the collision process is determined by the dynamics of a thin film that forms between the droplets as they come into contact. This introduces an enormous separation of length scales: Not only are the droplet diameters usually on a smaller length scale than the overall flow structures, but the thin film is typically several orders of magnitude thinner again than the droplet diameter. While the Euler-Euler and Euler-Lagrange methods fold all length scales into one by means of phenomenological collision models, the interface tracking and capturing methods have to resolve flow velocity and pressure all the way down to the scale of the film thickness. Thus, to resolve the interface correctly, many studies of droplet-droplet interaction using the VOF method have resorted to using adaptive mesh refinement to provide enough resolution to capture the dynamics of the thin film [17, 18, 19]. The very fine spatial resolution required renders these methods computationally expensive, however.

The motivation of the present work is to introduce a multi-scale model in which the thin film is resolved by a reduced-dimensional model. This eliminates the need to resolve the film thickness, while still maintaining direct numerical simulation of the bubble shape. Such methods sit between Euler-Euler or

2

Euler-Lagrange methods and the direct simulation approaches in terms of computational cost, but avoid the need for empirical correlations. This provides a more practical method to conduct direct simulations of collision processes, as well as to validate and calibrate higher-level phenomenological models from basic principles.

A few studies have already progressed in this direction. Kwakkel *et al.* [16] predict the moment of coalescence using the model of Zhang and Law [20], a system of ordinary differential equations derived to determine film drainage time. However, this model is restricted to head-on collision of identical droplets, and it was noted that it did not give a sufficiently accurate estimate of the film drainage time to produce an acceptable comparison with the experimental results [16]. A further step towards a more general, but still inexpensive model of coalescence was taken by Mason *et al.* [15], who applied a model for the thin film based on a Reynolds-type equation and coupled this to the fluid-flow model by prescribing velocity and thickness boundary conditions on the film equation based on the grid-scale model. The procedure uses cylindrical symmetry to reduce the film equation to a one-dimensional model, and a symmetry plane to prevent numerical coalescence. The numerical results were tested against one experimental result. Therefore, a more generic model that can be shown to consistently predict the collision outcome for a variety of collision regimes is still required.

In the present work, we have taken a similar approach to the one above. However, while the textbook application of the Reynolds equation solves for pressure given prescribed thickness or velocity boundaries, we develop a different approach in which the coupling is reversed. In addition, our aim is to produce a generic model which can work for the collision of dissimilar droplets moving in any manner relative to each other during the collision, rather than being restricted to head-on collision. The resulting method is demonstrated to be self-consistent across all four experiments which are available as validation data.

2. Flow model

The equations that govern incompressible immiscible droplets dispersed in a continuous fluid phase undergoing isothermal and laminar Newtonian three-dimensional flow are the volume averaged conservation of mass, momentum, and liquid-gas interface advection equations [2],

$$\nabla \cdot \mathbf{u} = 0, \tag{1}$$

$$\frac{\partial(\rho\mathbf{u})}{\partial t} + \nabla \cdot (\rho\mathbf{u}\mathbf{u}) = -\nabla p + \nabla \cdot (\mu\nabla\mathbf{u}) + \rho\mathbf{g} + \sum_{\theta=1}^{N} \sigma\kappa_\theta^s\nabla\alpha_\theta \tag{2}$$

and

$$\frac{\partial\alpha_\theta}{\partial t} + \nabla \cdot (\alpha_\theta\mathbf{u}) = 0 \tag{3}$$

3

where

$$\kappa_\theta^s = \nabla \cdot \frac{\nabla \alpha_\theta^s}{|\nabla \alpha_\theta^s|}, \tag{4}$$

$$\alpha_\theta^s - \alpha_\theta = \nabla^2 \left(\eta \alpha_\theta^s \right) \qquad \text{for } \theta \in \{1, 2, ..., N\}. \tag{5}$$

These equations describe N immiscible droplets dispersed in a continuous fluid phase with each droplet assigned a volume fraction field value $\alpha_1, \alpha_2, \ldots, \alpha_N$ in the range $[0, 1]$. Here ρ is the density, $\mathbf{u}$ the velocity, p the pressure, μ the dynamic viscosity, $\mathbf{g}$ the gravitational acceleration, and σ the coefficient of surface tension between the droplet and surrounding fluid. α_θ^s is a smoothed volume fraction field corresponding to each droplet, and κ_θ^s is the signed curvature calculated using the continuum surface force (CSF) method [21]. Smoothing of the volume fraction fields is achieved by solving equation (5), which is physically equivalent to solving a heat-conduction equation over a certain time interval starting with α_θ as the initial 'temperature' profile. The use of smoothed volume fraction fields improves the numerical calculation of second order gradients and thereby significantly reduces the errors in the calculation of the surface tension force using the CSF method [22]. Here, η represents the square of the characteristic smoothing length and will be discussed further in Section 4.5. The density, velocity, pressure and viscosity are cell averaged; for a quantity Φ:

$$\Phi = \sum_{\theta=1}^{N} \alpha_\theta \Phi_\theta + (1 - \sum_{\theta=1}^{N} \alpha_\theta)\Phi_0 \tag{6}$$

where Φ_0 corresponds to the continuous fluid phase surrounding the droplets.

The formulation above is known as the multiple marker VOF method, which uses separate indicator functions α_θ for each droplet and is essential to prevent premature numerical coalescence [2]. Although simple and straightforward to implement computationally, as it stands it is inadequate in that it prevents coalescence in all circumstances [2]. Thus, to model coalescence with this model, this work extends the method to include a reduced-order surface thin film model to predict the outcome of droplet-droplet collisions. Once coalescence is detected, the separate indicator functions are merged.

3. Coalescence model

The collision process between droplets can be described in three stages based on the film drainage theory of coalescence [23]. Consider two droplets: During Stage 1, they approach each other, and as they do so a thin film of the surrounding fluid is trapped between them as shown in Figure 1. In Stage 2, this fluid film drains out, and lastly in Stage 3 the droplets will either coalesce or bounce apart. The outcome depends on whether the thin film drains to a critical thickness h_c, at which point inter-molecular interactions across the film come into play, and it becomes unstable and ruptures [24]. This critical film thickness
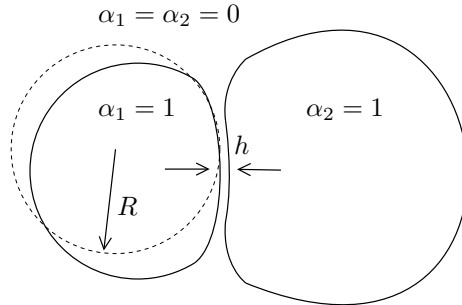
4

Figure 1: Formation of thin film between colliding droplets

is a characteristic of a given pair of fluids and is therefore considered to be a known quantity.

The thin film is thus an important aspect in modelling coalescence. The method developed here is aimed at modelling the dynamics of the thin liquid film during Stage 2 of the collision process. It calculates the film thickness and compares it to the critical thickness to decide whether coalescence should occur. Due to the extremely small scale of the thin film (typically, h_c is of the order of 10^{-8} m) a multiscale model is essential, where calculation of the film thickness occurs on the sub-grid scale.

It is known from lubrication theory [25] that the Reynolds equation describes the dynamics of a thin film between two moving interfaces. This can be derived based on the assumption that the film thickness h is much smaller than the smallest radius of curvature of the film surface, R ($h \ll R$). This implies that the surfaces of the two droplets, forming the bounding interfaces of the thin film, can be assumed to be locally planar at a given location in the thin film, though not necessarily parallel. This assumption leads by a standard procedure to the derivation of the Reynolds equation as detailed in Appendix A or for example by Hamrock *et al.* [26]. Considering a locally planar portion of the film where we define local co-ordinate axes X_i oriented such that X_2 is normal to the film, with the interfaces bounding the film located at $(X_1, X_2, X_3) = (0, \pm h/2, 0)$, dimensional analysis is used to show that the Navier-Stokes momentum equations (2) inside the thin film reduce to

$$\frac{\partial p}{\partial X_{1,3}} = \mu \frac{\partial^2 u_{1,3}}{\partial X_2^2} \tag{7}$$

and

$$\frac{\partial p}{\partial X_2} = 0, \tag{8}$$

i.e. that the viscous forces dominate over inertial and gravitational forces in the thin film. Here, u_i are the components of velocity in the directions of the X_i coordinate axes. Equations (7) imply that u_1 and u_3 have a quadratic profile with

5

respect to X_2 for $-h/2 \leq X_2 \leq h/2$. Applying boundary conditions $u_{1,3} = U_{1,3}^{(1)}$ at $X_2 = h/2$ and $u_{1,3} = U_{1,3}^{(2)}$ at $X_2 = -h/2$, where $U_i^{(1,2)}$ are the components of the boundary velocity at the film surfaces, yields

$$u_{1,3} = \frac{1}{2\mu} \frac{\partial p}{\partial X_{1,3}} \left(X_2^2 - \tfrac{1}{4}h^2 \right) + \frac{X_2}{h} \left(U_{1,3}^{(1)} - U_{1,3}^{(2)} \right) + \frac{1}{2} \left(U_{1,3}^{(1)} + U_{1,3}^{(2)} \right). \quad (9)$$

Inserting this velocity profile in the equation for mass conservation and integrating across the film thickness then leads to the well-known Reynolds equation

$$\frac{\partial(\rho h)}{\partial t} + h\frac{\partial}{\partial X_1} \left(\rho \frac{U_1^{(1)} + U_1^{(2)}}{2} \right) + h\frac{\partial}{\partial X_3} \left(\rho \frac{U_3^{(1)} + U_3^{(2)}}{2} \right)$$
$$- \frac{\partial}{\partial X_1} \left(\frac{\rho h^3}{12\mu} \frac{\partial p}{\partial X_1} \right) - \frac{\partial}{\partial X_3} \left(\frac{\rho h^3}{12\mu} \frac{\partial p}{\partial X_3} \right) = 0. \quad (10)$$

As a surface rather than a volume model, the Reynolds equation removes the need for numerical resolution across the film and constitutes the desired sub-grid model.

Returning to the original Cartesian co-ordinate system, and subject to the assumption $h \ll R$, equation (10) can be written as

$$\frac{\partial(\rho h)}{\partial t} + h\nabla \cdot \rho \left[\mathbf{Q} - (\mathbf{Q} \cdot \mathbf{n})\mathbf{n} \right] - \nabla \cdot \left[\frac{\rho h^3}{12\mu} \left[\nabla p - (\nabla p \cdot \mathbf{n})\mathbf{n} \right] \right] = 0, \quad (11)$$

where $\mathbf{n}$ is defined as the unit vector normal to the interface and

$$\mathbf{Q} = \frac{\mathbf{U}^{(1)} + \mathbf{U}^{(2)}}{2}, \quad (12)$$

is the average boundary velocity vector based on the velocities at the two droplet interfaces bounding the thin film.

4. Numerical implementation

The model equations are made up of equations (1)–(5) and (11)–(12). Equations (1)–(3) govern the flow between colliding droplets while equation (11) determines the outcome of the collision by evaluating the thickness of the thin liquid film.

In traditional applications of the Reynolds equation, (11) would be used to solve for pressure p given the time-variation of film thickness h. This approach is taken by Mason *et al.* [15] and by Harvie and Fletcher [27, 28], where the film thickness is obtained directly from the volume fraction field, and the film equation is used to solve for pressure. The coupling of the volume fraction to film thickness introduces a degree of algorithmic complexity [28], which is eased through the use of a symmetry plane at the coalescence boundary. In addition, the coupling of the film pressure back to the grid level solution is made more tractable by simulating only the liquid phase on the grid scale [15].

In search of a simpler and more generic method, we start from the intuition that the inter-droplet pressure should be determined, at least to a first approximation, by the momentum of the incoming droplets: Regardless of how well the flow in the thin film is resolved, the pressure must produce the reaction force necessary to decelerate them. More precisely, one can make the following argument: Consider that the pressure is approximately constant across the film thickness [equation (8)], and hence that the pressure in the film is equal to the pressure at the edges of the adjacent droplets, minus the surface-tension pressure jump. Since the pressure variation in the droplets is directly related to the velocity therein [according to equation (2)], it stands to reason that the thin film pressure can be directly related to the surrounding pressure at the edges of the droplets, provided the velocity field there is accurately represented. Thus, we do not need to know the velocity profile in the thin film, but only its effect on the surrounding droplets in the form of a lubrication force. The pressure inside the thin film can therefore correctly be extrapolated from the droplet edges after subtracting the surface-tension pressure-jump.

Thus, in the algorithm proposed here, we reverse the normal process of solving the Reynolds equation by solving for h based on pressure, and then feeding back a lubrication force to the boundaries of the droplets.

4.1. Initial droplet separation

The approach of solving equation (11) for film thickness requires an initial film thickness estimate h_0 to initialise the solution, as equation (11) is only valid when the droplets are close to each other. It is therefore necessary to devise a way to measure the initial separation distance h_0 between the droplets that is valid on the grid level (for separation of a few mesh cells or greater). For this purpose, a graphical approach based on measuring the distance from each droplet interface is used to approximate the separation h_0 between the particles.

Consider two interfaces that enclose fluids described by the volume fraction fields α_1 and α_2 which are close to each other in a computational domain. Consider lines which start from the interfaces pointing in the direction of the outward unit normal to the interfaces, $\mathbf{n}_1^s$ and $\mathbf{n}_2^s$, given by

$$\mathbf{n}_1^s = \frac{\nabla(\alpha_1^s)}{\mid \nabla(\alpha_1^s) \mid} \quad \text{and} \quad \mathbf{n}_2^s = \frac{\nabla(\alpha_2^s)}{\mid \nabla(\alpha_2^s) \mid}. \tag{13}$$

For a given point $\mathbf{x}$, we now measure the perpendicular distance to the surface of either droplet, at a point $\mathbf{x}_I^{(1,2)}$, by a path integral along a ray in the negative unit normal direction,

$$h_0^{(1)} = -\int_{\mathbf{x}}^{\mathbf{x}_I^{(1)}} (1 - \alpha_1)\mathbf{n}_1^s \cdot d\mathbf{l}, \tag{14}$$

and

$$h_0^{(2)} = -\int_{\mathbf{x}}^{\mathbf{x}_I^{(2)}} (1 - \alpha_2)\mathbf{n}_2^s \cdot d\mathbf{l}. \tag{15}$$
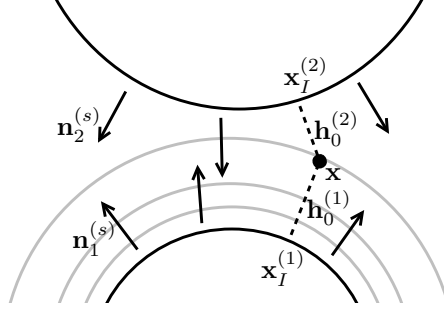
Figure 2: Method of approximating initial separation distance $h_0 = h_0^{(1)} + h_0^{(2)}$ at a given point $\mathbf{x}$. The faint lines represent equally spaced contours of $\alpha_1^{(s)}$ from which the normal vectors $\mathbf{n}_1^{(s)}$ are calculated

This is shown graphically in Figure 2.

In the region between the two interfaces, an estimate of the separation distance between the interfaces is

$$h_0 = h_0^{(1)} + h_0^{(2)}. \tag{16}$$

Since this gives the sum of the distance to interface 1 along the ray in direction $-\mathbf{n}_1^s$ and the distance to interface 2 along the ray in direction $-\mathbf{n}_2^s$ from any given point, the estimate becomes more accurate as the condition $h \ll R$ is approached and the interfaces become locally planar. This approach cannot however be used to obtain distances that are smaller than a mesh cell spacing; instead, the value of h_0 is used as an initial condition for the Reynolds equation (11).

In order to solve equations (14) and (15) using standard matrix solvers, we rewrite them in differential form. The equations for $h_0^{(1)}$ and $h_0^{(2)}$ now become

$$\nabla h_0^{(1)} \cdot \mathbf{n}_1^s = 1 - \alpha_1 \tag{17}$$

and

$$\nabla h_0^{(2)} \cdot \mathbf{n}_2^s = 1 - \alpha_2. \tag{18}$$

The differential form above is transparent to a uniform offset of $h_0^{(1)}$ or $h_0^{(2)}$, so to enforce the correct offset we peg the value inside the droplet to zero through the introduction of a binary switch,

$$[1 - H(\alpha_1 - 0.95)] \left(\nabla h_0^{(1)} \cdot \mathbf{n}_1^s \right) + H(\alpha_1 - 0.95) h_0^{(1)} = [1 - H(\alpha_1 - 0.95)] (1 - \alpha_1) \tag{19}$$

and

$$[1 - H(\alpha_2 - 0.95)] \left(\nabla h_0^{(2)} \cdot \mathbf{n}_2^s \right) + H(\alpha_2 - 0.95) h_0^{(2)} = [1 - H(\alpha_2 - 0.95)] (1 - \alpha_2). \tag{20}$$

Here the function $H(x)$ is the Heaviside step function,

$$H(x) = \begin{cases} 1 & x \geq 0, \\ 0 & x < 0. \end{cases} \tag{21}$$

Therefore, when $\alpha_1 > 0.95$ or $\alpha_2 > 0.95$ the equations reduce to $h_0^{(1)} = 0$ or $h_0^{(2)} = 0$ respectively, as required.

4.2. Discretisation method

A Finite Volume Method (FVM) of discretization is followed for the flow equations (1)–(5), where the integral form of the governing equations on a finite number of non-overlapping control volumes is used to obtain a system of coupled nonlinear equations. The discretisation procedure is standard [29] and will not be detailed here. Equation (11) is valid in the thin film only, but for efficiency we opt to solve it on the same grid, also using the FVM. This avoids the overhead of assembling a second, surface, grid as a 2D representation of the film. Finally, the initial separation estimation equations (19)–(20) can also be discretised using the FVM.

From the initial separation distance (16), a region in space can be calculated to determine where the Reynolds equation is activated. For this purpose we define a switch β that turns the computation of the Reynolds equation on when the separation estimate h_0 spans a few mesh cells and turns it off for larger separations. This restricts the calculation of the equation to areas that are very close to the thin film region. The boolean switch used to identify this region is defined by

$$\beta = H\left(\xi \delta x - h_0\right) H(\alpha_1^s - 0.001) H(\alpha_2^s - 0.001) \tag{22}$$

where ξ is a dimensionless parameter that determines the width of the region where the thin film equation is solved as a multiple of the mesh spacing δx. Since ξ determines the point at which the calculation of film thickness switches from the estimate calculated using (19)–(20) to the value h calculated from (11), we refer to it as the 'switchover parameter'. The factors $H(\alpha_1^s - 0.001) H(\alpha_2^s - 0.001)$ are used to exclude regions very far from the droplets where the interface normals (derived from the smoothed alpha fields) may not be accurately calculated and hence the initial separation estimate would be invalid.

Since the calculation of h is only carried out inside the thin film region β, a boundary condition must be applied for evaluation of the gradient of h at the edge of the film region. A zero-gradient condition is applied at the edges to be consistent with the fact that h should be a constant across the film.

The discretised form of equation (11) evaluated using an implicit Euler

scheme is given by

$$\beta_P \frac{h_P^{m+1} - h_P^m}{\Delta t} V_P + \beta_P h_P^{m+1} \sum_f \mathbf{A}_f \cdot (\mathbf{Q} - \mathbf{Q} \cdot \mathbf{n}\, \mathbf{n})_f$$

$$- \beta_P \frac{(h_P^{m+1})^3}{12\mu} \sum_f \mathbf{A}_f \cdot (\nabla p_t^s)_f^{m+1} - \beta_P \frac{(\nabla p_t^s)_P^{m+1}(h_P^{m+1})^2}{4\mu} \cdot \sum_f \mathbf{A}_f h_f^{m+1}$$

$$+ (1 - \beta_P)\left(h_P^{m+1} - h_{0P}^{m+1}\right) V_P = 0, \quad (23)$$

where subscript $(\cdot)_P$ and $(\cdot)_f$ are quantities evaluated at the cell centres and cell faces of the control volume (via linear interpolation where necessary), while $(\cdot)^{m+1}$ and $(\cdot)^m$ are values evaluated at the new and old time step. V_P is the volume of the computational control volume, and $\mathbf{A}_f$ is the surface area vector that points in the direction normal to the cell face. At the faces which span active ($\beta = 1$) and inactive ($\beta = 0$) cells, h_f is set to the active cell value instead of being interpolated, in order to satisfy the zero-gradient boundary condition. The final term in equation (23) causes the film thickness h to be set equal to the estimated film thickness outside the vicinity of the thin film. This causes h to be automatically initialised to the starting value of h_0 as the thin film region grows.

For notational simplicity the tangential pressure term has been assigned a new symbol, $\nabla p_t = \nabla p' - (\nabla p' \cdot \mathbf{n})\mathbf{n}$. Furthermore, in order to correctly represent the pressure gradient in the sub-grid region between the droplets, the surface tension pressure jump has been removed by subtracting the surface tension force from the pressure gradient as follows:

$$\nabla p' = \nabla p - \sum_{\theta=1}^{N} \sigma \kappa_\theta^s \nabla \alpha_\theta. \qquad (24)$$

Finally, a smoothing iteration is applied to ∇p_t in order to reduce artifacts caused by parasitic currents in the VOF method. This is accomplished in the same way as the smoothed volume fraction field equation (5), i.e. by solving

$$\nabla p_t^s - \nabla p_t = \nabla^2 \left(\eta \nabla p_t^s\right). \qquad (25)$$

The remaining gradient operators are discretised using the standard Green-Gauss discretisation.

4.3. Lubrication force

Since the distribution of fluid velocity across the thin film is known from equation (9), the traction on the droplet surfaces caused by the thin film lubrication force can be calculated. Following (7), the X_1 and X_3 components of traction on the surfaces at $X_2 = \pm h/2$ with normal vectors $(X_1, X_2, X_3) = (0, \mp1, 0)$ respectively, are given by

$$\tau_{1,3}\big|_{\pm h/2} = \mp\mu \frac{\partial u_{1,3}}{\partial X_2}\bigg|_{\pm h/2}. \qquad (26)$$

Substituting the expression for fluid velocity given by equation (9) into the above and expressing it as a vector, the traction on droplet (1) and (2) respectively is

$$\boldsymbol{\tau}^{(1),(2)} = -\frac{h}{2}\nabla_t p \mp \frac{\mu}{h}\left(\mathbf{U}_t^{(1)} - \mathbf{U}_t^{(2)}\right), \tag{27}$$

where $\mathbf{U}_t = \mathbf{U} - (\mathbf{U}\cdot\mathbf{n})\mathbf{n}$.

In the thin film region activated by the indicator function β, the lubrication force is added to the momentum equation in a manner similar to the CSF approximation of the surface tension, and replaces the viscous force term (which is inaccurate due to the inadequate resolution of the thin film in the grid-scale model). Accordingly, the momentum equation (2) is modified as follows:

$$\frac{\partial(\rho\mathbf{u})}{\partial t} + \nabla\cdot(\rho\mathbf{uu}) = -\nabla p + (1-\beta)\nabla\cdot(\mu\nabla\mathbf{u}) + \rho\mathbf{g} + \sum_{\theta=1}^{2}\left[\sigma\kappa_\theta^s\nabla\alpha_\theta + \beta\,\boldsymbol{\tau}^{(\theta)}\,|\nabla\alpha_\theta|\right] \tag{28}$$

(restricted to two droplets for clarity).

4.4. Surface velocity extrapolation

A further technical issue is the calculation of the field $\mathbf{Q}$, which represents the average of the droplet surface velocities at either side of the thin film. Since we are solving the volume-discretised Reynolds equation (23), $\mathbf{Q}$ must be available throughout the film region, even if there is a gap of one or more mesh cells between the droplets. To achieve this, the boundary velocities are extrapolated outward from the edges of the droplets along rays in the direction of the outward-pointing normals $\mathbf{n}_{1,2}^{(s)}$. This is performed using a similar procedure to the calculation of h_0 described in section 4.1. The extrapolation is described by the differential equations

$$\mathbf{n}_1^s\cdot\nabla\mathbf{U}^{(1)} = 0 \tag{29}$$

and

$$\mathbf{n}_2^s\cdot\nabla\mathbf{U}^{(2)} = 0, \tag{30}$$

where $\mathbf{U}^{(1),(2)}$ must be set equal to the fluid velocity $\mathbf{u}$ inside droplets 1 and 2 respectively. As in equations (19) and (20), this is achieved using a Heaviside step function as a switch, which leads to the following set of equations to be solved:

$$[1 - H(\alpha_1 - 0.95)]\,\mathbf{n}_1^s\cdot\nabla\mathbf{U}^{(1)} + H(\alpha_1 - 0.95)(\mathbf{U}^{(1)} - \mathbf{u}) = 0 \tag{31}$$

and

$$[1 - H(\alpha_2 - 0.95)]\,\mathbf{n}_2^s\cdot\nabla\mathbf{U}^{(2)} + H(\alpha_2 - 0.95)(\mathbf{U}^{(2)} - \mathbf{u}) = 0. \tag{32}$$

These equations are also discretised using the finite volume method.

4.5. Volume fraction smoothing

As argued in [22], the CSF method of calculating surface tension suffers from inaccuracies caused by the discontinuity of the volume fraction fields α_θ. Explicit smoothing methods have been used to ameliorate these effects [8, 30, 31], as well as the implicit method proposed in [22]. Intuitively, the smoothing should act over a few cells to be effective. In order to achieve this with a mesh-independent parameter, we replace η at each cell face in the discretised version of equation (5) with

$$\eta = [\chi(\boldsymbol{\delta} \cdot \mathbf{n}_f)]^2 \tag{33}$$

where $\boldsymbol{\delta}$ is the vector joining the two adjacent cell centres, and $\mathbf{n}_f$ is the unit normal to the face. χ is a user-selectable constant determining the smoothing length as a multiple of the cell spacing.

4.6. Solution procedure

A summary of the overall solution procedure is as follows:

- Calculate the velocity fluxes and advect the multiple VOF fields by solving equation (3).

- Solve for smoothed volume fraction fields and curvature [equations (5) and (4)].

- Using the pressure correction algorithm PISO [32], solve the pressure equation derived from the continuity equation (1), and solve the momentum equation (28) to determine velocity.

- Calculate initial separation distance h_0 by solving equations (19) and (20).

- Where h_0 is smaller than a certain number of mesh cells, ξ:

    - Extrapolate boundary velocities by solving equations (31) and (32).
    - Solve the reduced-order surface thin film equation (23) to obtain h.
    - If $\min(h) < h_c$, merge the volume fraction fields.

- Where h_0 is greater than ξ mesh cells:

    - Set $h = h_0$.
    - Do not solve the reduced order surface thin film equations.

- Move on to the next time-step and repeat until final time is reached.

The VOF field equations (3) are solved explicitly using the MULES interface-capturing method of OpenFOAM [33]. The remaining discretised equations are solved using the algebraic multigrid matrix solver provided by OpenFOAM.
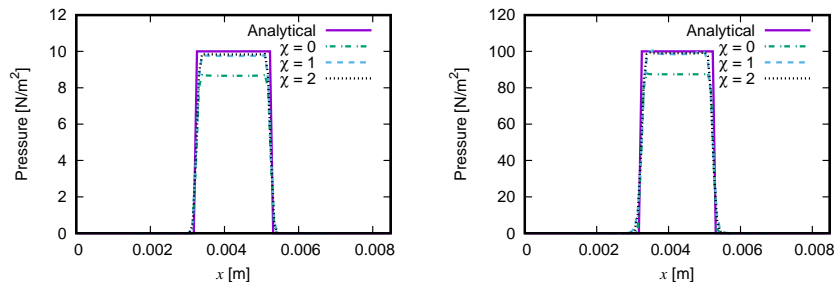
Figure 3: Pressure profile across stationary droplet for $\sigma = 0.01$ kg s^{-2} (left) and $\sigma = 0.1$ kg s^{-2} (right), for various smoothing parameters.

5. Numerical evaluation

5.1. Selection of volume fraction smoothing parameter χ

In order to evaluate the effect of the smoothing length χ, we simulate a 2D stationary droplet with radius $R = 1$ mm, density $\rho_l = 1000$ kg/m^3 and viscosity $\mu_l = 1 \times 10^{-3}$ kg/m/s suspended in a gas with density $\rho_g = 1$ kg/m and viscosity $\mu_g = 1.5 \times 10^{-5}$ kg/m/s. Two different surface tension coefficients are used: $\sigma = 0.01$ kg s^{-2} and 0.1 kg s^{-2}. The orthogonal mesh consists of 40 cells across the droplet diameter.

After 0.05 s of simulation time, the pressure increment across the surface of the droplet is compared to the known analytical solution, given by the Young-Laplace equation [34]:

$$\Delta p = \sigma \kappa \tag{34}$$

where the curvature κ is given by $\kappa = 1/R$ in two dimensions. The results are shown in Figure 3 for the two surface tension coefficients and for $\chi = 0, 1$ and 2. There is a clear discrepancy of approximately 13% for the predicted pressure jump in the unsmoothed case ($\chi = 0$), while the predicted pressure jumps for $\chi = 1$ and 2 are within 2.5% of the true value.

We wish to make the smoothing large enough to eliminate mesh-scale inaccuracies caused by the discontinuity of the volume fraction fields α_θ, but not so large as to smooth out genuine interface deformations on the scale of the smoothing length. The results of Figure 3 support the intuition that smoothing on the scale of one or two mesh cells is sufficient to significantly improve the accuracy of the CSF method. Therefore, to avoid the risk of over-smoothing, we select $\chi = 2$ for the remainder of this study.

5.2. Experimental and numerical set-up for evaluation of droplet collision

In the remainder of this section, the implementation of the reduced order surface thin film model coupled to the multiple marker VOF method is tested against the experiment described by Pan, Law and Zhou in [13]. The experiment provides detailed time resolved interface deformation images of the head on

	Liquid (Tetradecane)	Gas (Nitrogen)
Density ρ $(\mathrm{kg\,m^{-3}})$	762	1.225
Viscosity μ (kg/m/s)	2.13×10^{-3}	1.76×10^{-4}
Surface Tension σ $(\mathrm{kg\,s^{-2}})$	0.0265	

Table 1: Material Properties for Tetradecane and Nitrogen at $20°$C

Quantity	Case I	Case II	Case III	Case IV
U_0 $(\mathrm{m\,s^{-1}})$	0.302	0.24	0.496	0.596
R $(\mu\mathrm{m})$	107.2	170.6	167.6	169.7
We	2.25	2.26	9.33	13.63
T (ms)	0.415	0.831	0.811	0.826

Table 2: Experimental parameters for the four test cases presented in [13]

collision of two identical Tetradecane ($C_{14}H_{30}$) droplets in 1 atm Nitrogen gas. The material properties are shown in Table 1.

The four test cases described in [13] are studied. We refer to these as Case I – Case IV as they are presented in [13]. The first two result in droplet coalescence and rebound (respectively) with minimal droplet deformation while the last two produce rebound and coalescence with large deformations in the droplet shapes. They are specifically selected to be close to the transition between the two behaviours, and therefore provide a stringent test of any model seeking to describe the process consistently. The experimental parameters, viz. individual droplet velocity U_0 (half their relative approach velocity), droplet radius R, Weber number $We = 4\rho_l U_0^2 R/\sigma$, and droplet oscillation period $T = 2\pi\sqrt{\rho_l R^3/8\sigma}$, are shown in Table 2 for each test case. Here ρ_l is the density of Tetradecane.

Since the radii of the droplets is $O(10^{-3}\,\mathrm{m})$, gravity is negligible compared to surface tension forces and the term $\rho\mathbf{g}$ in the momentum equation is neglected. The simulations are performed on an axisymmetric structured, Cartesian and uniform mesh. The domain dimensions are $5D \times 2D$ where D is the corresponding droplet diameter, and an initial mesh size of 720×160 elements is used, i.e. $O(100)$ elements across the droplet diameter.

Since the known approach velocity is measured at the time when the droplets have a separation of approximately $1.5D$, we initialise the numerical simulation with a separation of $1.5D$ and the liquid velocity set uniformly to the prescribed initial value. It is noted that the velocity field in the droplets and surrounding gas adjusts to a steady profile in a time much shorter than the droplets take to meet, and that the overall droplet velocity is not perceptibly changed during this initial settling period.

The boundary conditions for the pressure are set to zero gradient at the walls with an internal air pressure set to 1 atm. A no-slip velocity boundary condition is set at the walls with an initial internal gas velocity of zero and velocity within each droplet set to U_0.

5.3. Selection of switch-over parameter ξ

In the determination of the thin film region β, the numerical parameter ξ is required to determine the mesh cell spacing at which to switch from the geometric determination of the initial separation h_0 to the solution h of the surface thin film model. It is essential that the results are not sensitive to the value of ξ used in the simulations. If it is too small, then the results will be corrupted by the finite mesh resolution of the inter-droplet region. On the other hand, it should not be larger than necessary so that the assumption $h \ll R$ is satisfied as closely as possible.

Therefore, to determine an appropriate value of ξ, we observe the results of Case IV with ξ varied from 3 to 8. For the purpose of this assessment we set $h_c = 0$ to inhibit coalescence and observe the Reynolds equation being solved for the duration of the contact between the droplets. We have selected Case IV for this experiment as it is the most dynamic case, expected to present the most stringent test. Figure 4 shows the minimum film thickness across the domain (denoted h_{Min}) attained for different values of ξ. Between $\xi = 6$ to $\xi = 8$ the value of h_{Min} changes by less than 1% and therefore the value $\xi = 7$ is selected as sufficiently large.
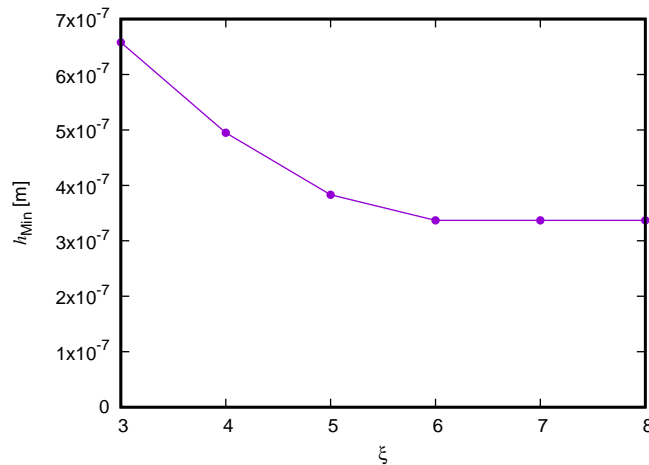

Figure 4: Minimum film thickness h_{Min} for Case IV, as a function of switchover point from estimated to computed film thickness

5.4. Mesh dependence

To evaluate the mesh dependence of the model, we consider the same Case IV described above, where the minimum film thickness is plotted as a function of time for four different meshes. We start with a coarse mesh of 270×60 elements (approx 30 elements across the bubble diameter), repeatedly reducing the mesh spacing by a factor of $1/\sqrt{2}$ to produce 'Medium', 'Fine' and 'Finer' meshes. The results are shown in Figure 5.
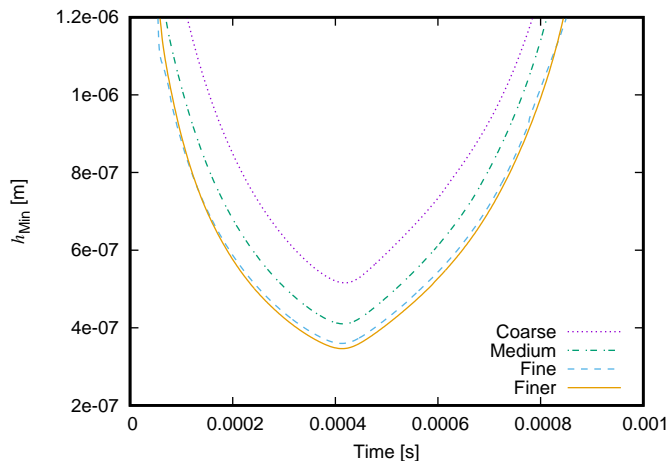
15

Figure 5: Minimum film thickness h_{Min} as a function of time for Case IV, for various mesh densities

Whilst showing, predictably, some dependence of the result on mesh resolution, these results indicate convergence to a final value of the minimum film thickness. The 'Finer' mesh was used in the subsequent analyses.

5.5. Critical film thickness

The one physical parameter present in the model is the critical film thickness h_c at which film rupture, and therefore coalescence, occur. This is assumed to be a universal parameter for a given pair of fluids, but is not known beforehand. We therefore use the first experiment as a calibration, setting h_c to achieve the best correspondence with the numerical results, and then use the other three experiments to test the model.

Similar to the determination of ξ, h_c is initially set to zero and the numerical results at $\xi = 7$ are obtained for the four test cases, using the 'Finer' computational mesh. The results are shown in Figure 6. In order to achieve coalescence in the first experiment, a value $h_c \geq 4.36 \times 10^{-7}$m is sought. Starting from this value, we run the simulation again and compare the interface deformation snapshots, adjusting h_c until the best correspondence is achieved.

5.6. Interface deformation

The time series interface deformation plots of the droplets for Case I are shown in Figure 7, and compared to the experimentally obtained photographs presented in [13]. The value of h_c used to generate Figure 7 is 4.37×10^{-7}m, which yielded the best comparison between experimental and numerical results for that case. Cases II-IV were then simulated with the same value of h_c, and the results shown in Figures 8–10.
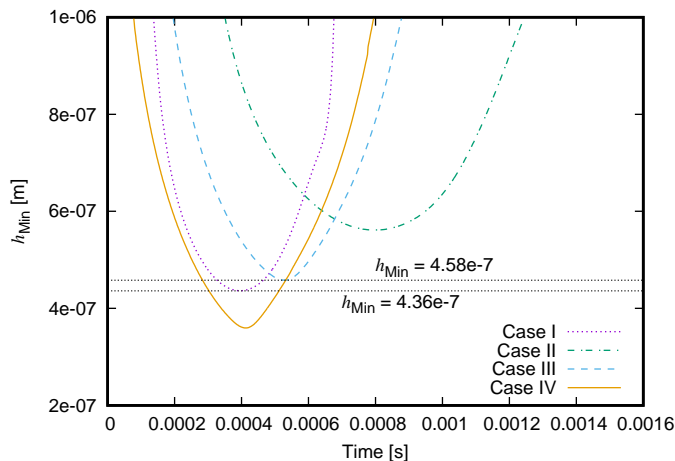
16

Figure 6: Minimum film thickness h_{Min} as a function of time for Cases I-IV

The interface deformation shows excellent agreement throughout the simulation time for both the calibration simulation (Case I) and the validation tests (Cases II-IV). In particular, the moment of coalescence can be seen to be very accurately predicted in Case IV (two panels at bottom left of Figure 10), and the absence thereof correctly predicted in Cases II and III. The numerical results are obtained at a reasonable computational cost without the need to excessively refine the computational mesh.

5.7. Comparison with other studies

Several other studies have compared against the same set of experimental data. Pan *et al.* [13] calculated the minimum film thickness for the cases resulting in merging to be 2×10^{-7} m. This is in fairly close agreement with the value arrived at here of 3.37×10^{-7} m. By contrast, in the work of Mason *et al.* [15] a critical film thickness of 0.4×10^{-7} m obtained agreement with the results referred to as Case IV above, and did not consider the other three test cases. Chen and Yang [35] used the head-on collision resulting in bouncing to test their adaptive mesh refinement technique using an axisymmetric simulation. The minimum cell spacing used in their simulations was roughly 1.5×10^{-8} m and a minimum gas film thickness of 3×10^{-7} m was calculated, also in good agreement with the results obtained here where a minimum mesh cell spacing of roughly 1.2×10^{-6} m – two orders of magnitude larger – could be used thanks to the multiscale approach.

In [13], it is discussed that the actual film thickness at which breakup should occur due to Van Der Waal's forces coming into play, is an order of magnitude smaller than that which is predicted by continuum models, such as the present one and those discussed above. This is due to the film thickness becoming small compared to the molecular mean free path, rendering the continuum formulation
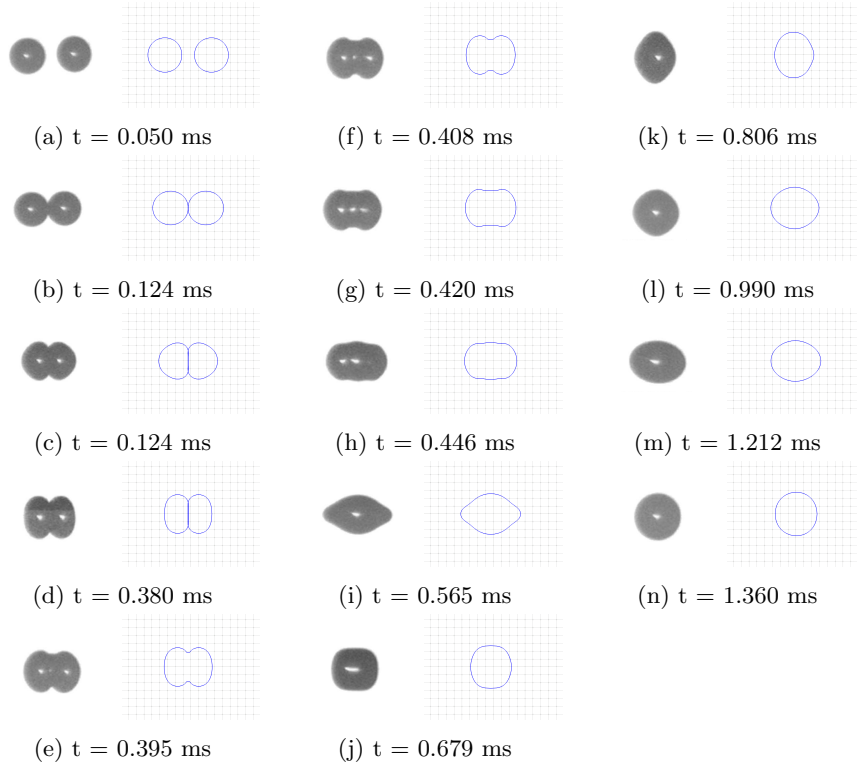
Figure 7: Time series interface shape deformations for Case I, showing experimental snapshots from [13] (L) and numerical computations (R). A grid of 50 μm is shown for scale.

inaccurate at very small film thickness. Nonetheless, it is argued in [13] that the continuum formulation holds predictive power, and the results presented here support this. The quantity h_c, however, needs to be interpreted merely as a parameter of the model, without a direct physical interpretation.

A method of compensating for the inaccuracy in the continuum formulation is presented in the related work of Harvie and Fletcher [27], whereby a partial-slip velocity boundary condition is used at the film surface. However, in [15], a no-slip boundary is used, as in the present work, and therefore this does not account for the discrepancy in the results compared to the present work as well as the other continuum models discussed above – even though it is closer to the result that would be expected if non-continuum effects were accounted for. In [15] it is discussed that parasitic currents stemming from the CSF surface-tension formulation are seen to increase with increasing mesh refinement. This could make it difficult to obtain a mesh independent result. Additionally, since the film thickness is directly obtained from the volume fraction arrangement in the volume-of-fluid mesh, it is possible that this would be disturbed appreciably by spurious currents on the surface of the droplet. The inverse coupling arrangement presented in this paper, by contrast, is not sensitive to the precise
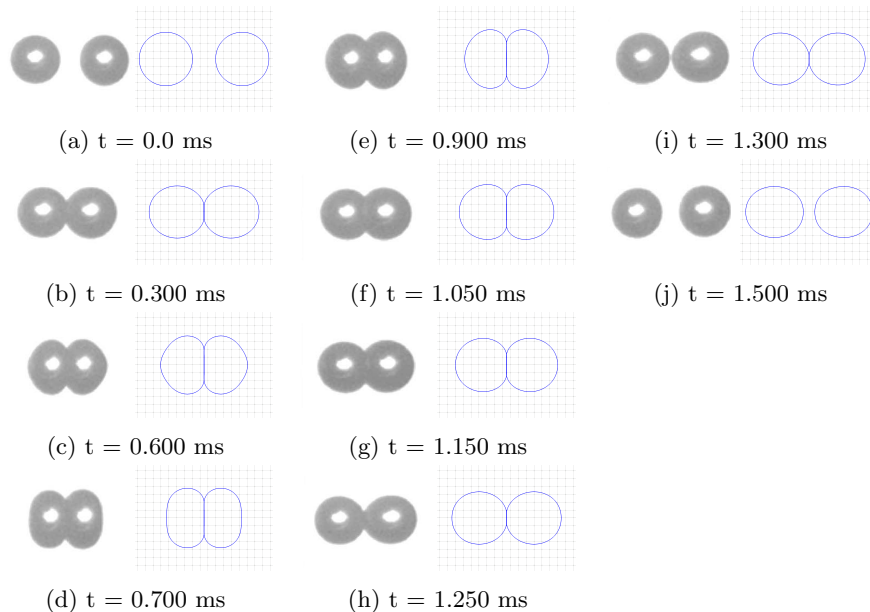
18

Figure 8: Time series interface shape deformations for Case II, showing experimental snapshots from [13] (L) and numerical computations (R). A grid of 50 μm is shown for scale.

separation of the volume fraction fields since it is coupled via the pressure which, it has been argued, is a better behaved quantity for the purpose.

6. Conclusion

To model droplet-droplet coalescence a reduced-order surface thin film model coupled to a multiple marker VOF method was presented. The model was derived based on the thin film drainage theory which assumes the presence of a gas film between interacting droplets and takes the form of a Reynolds equation. The governing set of equations was discretised using a FVM and a numerical solution obtained using an implicit scheme with pressure correction. The implementation in this study uses the pressure from the Navier-Stokes equations as an input into the thin-film model. The film model is initialised with a grid-scale film thickness and thereafter allowed to solve on the sub-grid scale with pressure as the only input. This is in contrast to the otherwise similar technique of Mason *et al.* [15] where velocity boundary conditions from the grid-scale flow model are applied to the film model, which is then used to solve for pressure.

The method was tested by simulating the binary collision of identical Tetrade-cane droplets in 1 atm. Nitrogen and demonstrated the predictive power of the surface thin film model. Although the critical film thickness was set based on the first experimental datum, the results showed excellent agreement with the

(a) t = 0.300 ms   (g) t = 0.790 ms   (m) t = 1.100 ms

(b) t = 0.470 ms   (h) t = 0.850 ms   (n) t = 1.200 ms

(c) t = 0.500 ms   (i) t = 0.905 ms   (o) t = 1.285 ms

(d) t = 0.600 ms   (j) t = 0.950 ms   (p) t = 1.400 ms

(e) t = 0.650 ms   (k) t = 1.000 ms
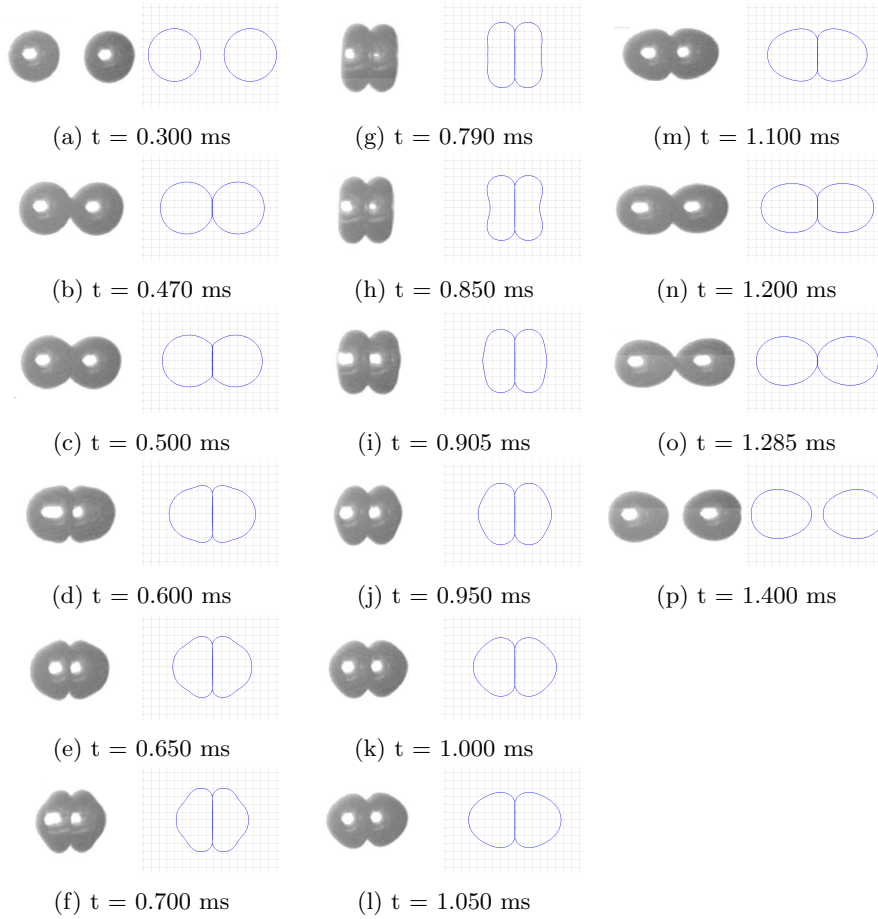
(f) t = 0.700 ms   (l) t = 1.050 ms

Figure 9: Time series interface shape deformations for Case III, showing experimental snapshots from [13] (L) and numerical computations (R). A grid of 50 μm is shown for scale.

other three experiments of Pan *et al.* [13] under different collision conditions. The method was shown to accurately predict the deformation of the droplets for the duration of the collisions.

Although this method has been described and validated for droplets (i.e. liquids suspended in a gas phase), it is also applicable if the phases are reversed and colliding bubbles are considered. Bubble coalescence has a significant impact on the performance of bubble-column reactors [36], among other industrial processes. In addition, this method would be applicable with slight modifications to analyse the thin film trapped between a droplet and a wall, and therefore the smearing or rebound behaviour of the droplets. This is of interest in modelling the behaviour of fuel in combustion chambers [3].
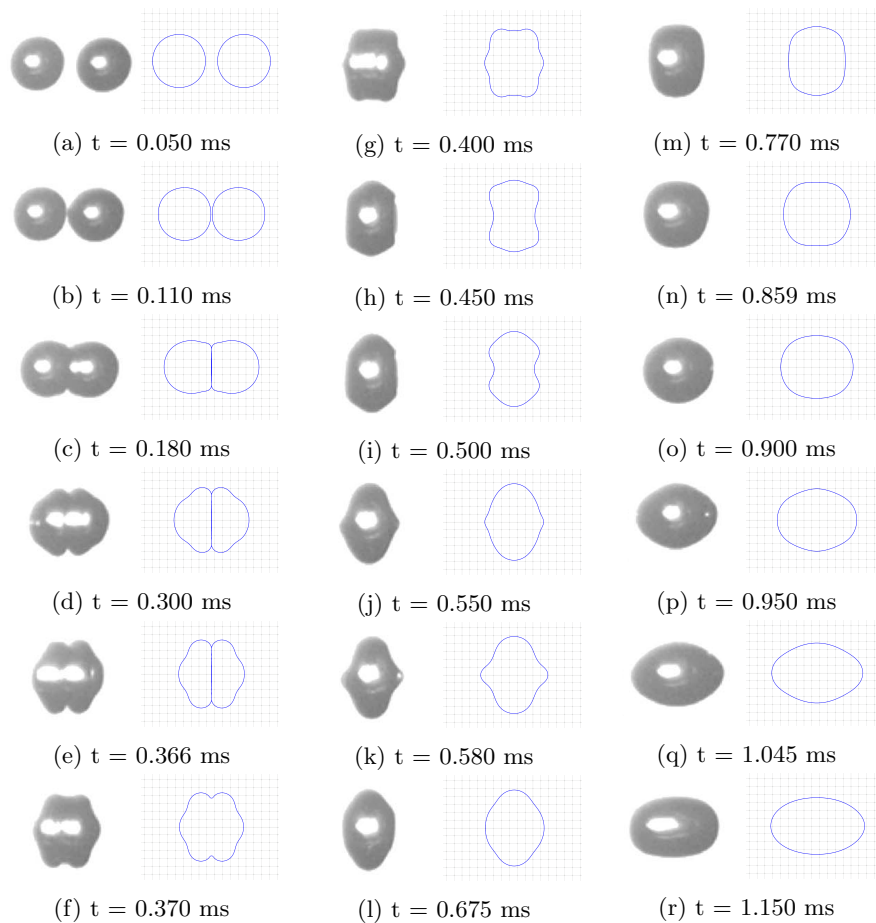
Figure 10: Time series interface shape deformations for Case IV, showing experimental snapshots from [13] (L) and numerical computations (R). A grid of 50 μm is shown for scale. The apparent discrepancy in panels (h) and (i) can be explained by the fact that the photographs capture a silhouette rather than the slice shown on the right.

7. Acknowledgements

Appendix A. Derivation of Reynolds equation

It is assumed that the film thickness h is small, specifically that it is everywhere much smaller than the local radius of curvature of the film surface, R: ($h \ll R$). Thus, the film surfaces are locally planar, and at any given location we define local co-ordinate axes X_i oriented such that X_2 is in the direction of the mean of the normals of the interfaces bounding the film, and the interfaces are located at $(X_1, X_2, X_3) = (0, \pm h/2, 0)$. $U_i^{(1,2)}$ are the components of the boundary velocity at $X_2 = \pm h/2$ respectively.

Starting from the Navier-Stokes momentum equations (2), in the three co-ordinate directions with $i = 1 \ldots 3$ these become

$$\rho \left(\frac{\partial u_i}{\partial t} + u_1 \frac{\partial u_i}{\partial X_1} + u_2 \frac{\partial u_i}{\partial X_2} + u_3 \frac{\partial u_i}{\partial X_3} \right) = -\frac{\partial p}{\partial X_i} + \mu \left(\frac{\partial^2 u_i}{\partial X_1^2} + \frac{\partial^2 u_i}{\partial X_2^2} + \frac{\partial^2 u_i}{\partial X_3^2} \right) + \rho g_i. \tag{A.1}$$

Dimensional analysis is used to determine which terms in the above equations dominate. Let the characteristic length in the X_1 and X_3 directions be given by the radius R of the droplet, and the characteristic length in the X_2 direction by the film thickness h. Let U denote the characteristic velocity magnitude, and the characteristic time be R/U. The characteristic pressure used is the pressure drop for Poiseuille flow, $\mu V R/h^2$. The equations (A.1) in non-dimensional form are then given by:

$$Re \left(\frac{\partial u_{1,3}^*}{\partial t^*} + u_1^* \frac{\partial u_{1,3}^*}{\partial X_1^*} + \frac{R}{h} u_2^* \frac{\partial u_{1,3}^*}{\partial X_2^*} + u_3^* \frac{\partial u_{1,3}^*}{\partial X_3^*} \right) =$$
$$-\frac{R^2}{h^2} \frac{\partial p^*}{\partial X_{1,3}^*} + \frac{\partial^2 u_{1,3}^*}{\partial X_1^{*2}} + \frac{R^2}{h^2} \frac{\partial^2 u_{1,3}^*}{\partial X_2^{*2}} + \frac{\partial^2 u_{1,3}^*}{\partial X_3^{*2}} + \frac{\rho g_{1,3} R^2}{\mu U} \quad \text{(A.2)}$$

(X_1, X_3 components), and

$$Re \left(\frac{\partial u_2^*}{\partial t^*} + u_1^* \frac{\partial u_2^*}{\partial X_1^*} + \frac{R}{h} u_2^* \frac{\partial u_2^*}{\partial X_2^*} + u_3^* \frac{\partial u_2^*}{\partial X_3^*} \right) =$$
$$-\frac{R^3}{h^3} \frac{\partial p^*}{\partial X_2^*} + \frac{\partial^2 u_2^*}{\partial X_1^{*2}} + \frac{R^2}{h^2} \frac{\partial^2 u_2^*}{\partial X_2^{*2}} + \frac{\partial^2 u_2^*}{\partial X_3^{*2}} + \frac{\rho g_2 R^2}{\mu U} \quad \text{(A.3)}$$

(X_2 component), where the starred quantities are non-dimensional variables approximately of order 1 in magnitude, and $Re = \rho U R/\mu$ is the Reynolds number. Therefore, in the limiting case of $h \ll R$, (A.2) and (A.3) reduce to equations (7) and (8) already presented in Section 3, and with the resulting velocity profile given in terms of pressure by equation (9).

The continuity equation $\frac{\partial \rho}{\partial t} + \frac{\partial \rho u_i}{\partial X_i} = 0$ is now included in order to close the system of equations, being integrated across the film from $X_2 = -h/2$ to $X_2 = h/2$ to give

$$\int_{-h/2}^{h/2} \frac{\partial \rho}{\partial t} dX_2 + \int_{-h/2}^{h/2} \frac{\partial \rho u_1}{\partial X_1} dX_2 + \rho u_2 \Big|_{-h/2}^{h/2} + \int_{-h/2}^{h/2} \frac{\partial \rho u_3}{\partial X_3} dX_2 = 0. \tag{A.4}$$

Applying the Leibniz integral rule, $\frac{\partial}{\partial x} \int_a^b f(x,y)dy = f(x,b)\frac{\partial b}{\partial x} - f(x,a)\frac{\partial a}{\partial x} + \int_a^b \frac{\partial f}{\partial x}dy$, and assuming that density remains constant across the film, we obtain

$$\frac{\partial \rho}{\partial t}h + \frac{\partial M_1}{\partial X_1} - \rho\frac{U_1^{(1)} + U_1^{(2)}}{2}\frac{\partial h}{\partial X_1} + \rho\left(U_2^{(1)} - U_2^{(2)}\right) + \frac{\partial M_3}{\partial X_3} - \rho\frac{U_3^{(1)} + U_3^{(2)}}{2}\frac{\partial h}{\partial X_3} = 0$$
$$(A.5)$$

where $M_1 = \int_{-h/2}^{h/2} \rho u_1 dX_2$ and $M_3 = \int_{-h/2}^{h/2} \rho u_3 dX_2$ are the mass flow rates in the X_1 and X_3 directions. These can be determined from the previously obtained expressions (9) for u_1 and u_3 to obtain

$$M_{1,3} = -\frac{\rho h^3}{12\mu}\frac{\partial p}{\partial X_{1,3}} + \rho\frac{U_{1,3}^{(1)} + U_{1,3}^{(2)}}{2}h. \qquad (A.6)$$

Finally, substituting expressions (A.6) into (A.5) and observing that $U_1^{(1)} - U_1^{(2)} = \frac{\partial h}{\partial t}$, yields the final form of the Reynolds equation (10):

$$\frac{\partial(\rho h)}{\partial t} + h\frac{\partial}{\partial X_1}\left(\rho\frac{U_1^{(1)} + U_1^{(2)}}{2}\right) + h\frac{\partial}{\partial X_3}\left(\rho\frac{U_3^{(1)} + U_3^{(2)}}{2}\right)$$
$$- \frac{\partial}{\partial X_1}\left(\frac{\rho h^3}{12\mu}\frac{\partial p}{\partial X_1}\right) - \frac{\partial}{\partial X_3}\left(\frac{\rho h^3}{12\mu}\frac{\partial p}{\partial X_3}\right) = 0.$$

References

[1] C. Hirt, B. Nichols, Volume of fluid (VOF) method for the dynamics of free boundaries, Journal of Computational Physics 39 (1) (1981) 201–225.

[2] E. Coyajee, B. Boersma, Numerical simulation of drop impact on a liquid-liquid interface with a multiple marker front-capturing method, Journal of Computational Physics 228 (12) (2009) 4444–4467.

[3] A. Murrone, P. Villedieu, Numerical modeling of dispersed two-phase flows, Aerospace Lab 2 (2) (2011) 1–13.

[4] Y. Shi, H. Ge, R. Reitz, Computational Optimization of Internal Combustion Engines, SpringerLink : Bücher, Springer London, 2011.

[5] R. Kuriakose, C. Anandharamakrishnan, Computational fluid dynamics (CFD) applications in spray drying of food products, Trends in Food Science & Technology 21 (8) (2010) 383–398.

[6] H. Jakobsen, H. Lindborg, C. Dorao, Modeling of bubble column reactors: Progress and limitations, Industrial & Engineering Chemistry Research 44 (14) (2005) 5107–5151.

[7] M. Nobari, Y. Jan, G. Tryggvason, Head-on collision of drops–a numerical investigation., Physics of Fluids 8 (1) (1996) 29.

[8] S. J. Cummins, M. M. Francois, D. B. Kothe, Estimating curvature from volume fractions, Computers & Structures 83 (67) (2005) 425–434.

[9] B. Lafaurie, C. Nardone, R. Scardovelli, S. Zaleski, G. Zanetti, Modelling merging and fragmentation in multiphase flows with SURFER, Journal of Computational Physics 113 (1) (1994) 134–147.

[10] D. Harvie, M. Davidson, M. Rudman, An analysis of parasitic current generation in volume of fluid simulations, Applied Mathematical Modelling 30 (10) (2006) 1056–1066.

[11] F. Denner, D. R. van der Heul, G. T. Oud, M. M. Villar, A. da Silveira Neto, B. G. van Wachem, Comparative study of mass-conserving interface capturing frameworks for two-phase flows with surface tension, International Journal of Multiphase Flow 61 (2014) 37–47.

[12] A. Tomiyama, A. Sou, H. Minagawa, T. Sakaguchi, Numerical analysis of a single bubble by VOF method, JSME International Journal Series B 36 (1) (1993) 51–56.

[13] K.-L. Pan, C. Law, B. Zhou, Experimental and mechanistic description of merging and bouncing in head-on binary droplet collision, Journal of Applied Physics 103 (6) (2008) 064901.

[14] X. Li, U. Fritsching, Numerical investigation of binary droplet collisions in all relevant collision regimes, Journal of Computational Multiphase Flows 3 (4) (2011) 207–224.

[15] L. Mason, G. Stevens, D. Harvie, Multi-scale volume of fluid modelling of droplet coalescence, in: Ninth International Conference on CFD in the Minerals and Process Industries, 2012.

[16] M. Kwakkel, W.-P. Breugem, B. J. Boersma, Extension of a CLSVOF method for droplet-laden flows with a coalescence/breakup model, Journal of Computational Physics 253 (2013) 166–188.

[17] N. Nikolopoulos, A. Theodorakakos, G. Bergeles, Off-centre binary collision of droplets: A numerical investigation, International Journal of Heat and Mass Transfer 52 (19-20) (2009) 4160–4174.

[18] N. Nikolopoulos, G. Strotos, K. Nikas, G. Bergeles, The effect of Weber number on the central binary collision outcome between unequal-sized droplets, International Journal of Heat and Mass Transfer 55 (7-8) (2012) 2137–2150.

[19] A. Albadawi, D. Donoghue, A. Robinson, D. Murray, Y. Delauré, On the assessment of a VOF based compressive interface capturing scheme for the analysis of bubble impact on and bounce from a flat horizontal surface, International Journal of Multiphase Flow 65 (2014) 82–97.

[20] P. Zhang, C. K. Law, An analysis of head-on droplet collision with large deformation in gaseous medium, Physics of Fluids 23 (4) (2011) 042102.

[21] J. Brackbill, D. Kothe, C. Zemach, A continuum method for modeling surface tension, Journal of Computational Physics 100 (2) (1992) 335–354.

[22] J. Heyns, O. Oxtoby, Modelling surface tension dominated multiphase flows using the VOF approach, in: 6th European Conference on Computational Fluid Dynamics, 2014, pp. 7082–7090.

[23] J.-D. Chen, P. Hahn, J. Slattery, Coalescence time for a small drop or bubble at a fluid-fluid interface, American Institute of Chemical Engineers Journal 30 (4) (1984) 622–630.

[24] G. D. Mackay, S. G. Mason, The gravity approach and coalescence of fluid drops at liquid interfaces, Canadian Journal of Chemical Engineering 41 (1963) 203–212.

[25] J.-D. Chen, A model of coalescence between two equal-sized spherical drops or bubbles, Journal of Colloid and Interface Science 107 (1) (1985) 209–220.

[26] B. J. Hamrock, S. R. Schmid, B. O. Jacobson, Fundamentals of Fluid Film Lubrication, Second Edition, Marcel Dekker, 2004.

[27] D. J. Harvie, D. F. Fletcher, A hydrodynamic and thermodynamic simulation of droplet impacts on hot surfaces, Part I: theoretical model, International Journal of Heat and Mass Transfer 44 (2001) 2633–2642.

[28] D. J. E. Harvie, A hydrodynamic and thermodynamic simulation of droplet impacts on hot surfaces, Ph.D. thesis, University of Sydney (1999).

[29] O. Oxtoby, A. Malan, J. Heyns, A computationally efficient 3D finite-volume scheme for violent liquid–gas sloshing, International Journal for Numerical Methods in Fluids 79 (2015) 306–321.

[30] M. Williams, D. Kothe, E. Puckett, Convergence and accuracy of kernel-based continuum surface tension models, Tech. rep., Los Alamos National Lab., NM (US) (1998).

[31] O. Ubbink, Numerical prediction of two fluid systems with sharp interfaces, Ph.D. thesis, University of London (1997).

[32] R. Issa, Solution of the implicitly discretised fluid flow equations by operator-splitting, Journal of Computational Physics 62 (1) (1986) 40–65.

[33] H. G. Weller, G. Tabor, H. Jasak, C. Fureby, A tensorial approach to computational continuum mechanics using object-oriented techniques, Computers in Physics 12 (1998) 620–631.

[34] F. M. White, Fluid Mechanics, 5th Edition, McGraw-Hill, Boston, 2003.

[35] X. Chen, V. Yang, Thickness-based adaptive mesh refinement methods for multi-phase flow simulations with thin regions, Journal of Computational Physics 269 (2014) 22–39.

[36] H. Jakobsen, Bubble Column Reactors, Springer International Publishing, 2014, pp. 883–935.